Chinese Journal of Catalysis 41 (2020) 1745–1753

available at www.sciencedirect.com

ScienceDirect

journal homepage: www.elsevier.com/locate/chnjc

Article

Dissolution-regrowth of hierarchical Fe-Dy oxide modulates the electronic structure of nickel-organic frameworks as highly active and stable water splitting electrocatalysts

Zixia Wan [a], Qiuting He [a], Jundan Chen [a], Tayirjan Taylor Isimjan [c,$], Bao Wang [b,#], Xiulin Yang [a,*]

[a] *Guangxi Key Laboratory of Low Carbon Energy Materials, School of Chemistry and Pharmaceutical Sciences, Guangxi Normal University, Guilin 541004, Guangxi, China*

[b] *State Key Laboratory of Biochemical Engineering, Institute of Process Engineering, Chinese Academy of Sciences, Beijing 100190, China*

[c] *Saudi Arabia Basic Industries Corporation (SABIC) at King Abdullah University of Science and Technology (KAUST), Thuwal 23955-6900, Saudi Arabia*

ARTICLE INFO

Article history:
Received 26 February 2020
Accepted 31 March 2020
Published 5 November 2020

Keywords:
Metal-organic frameworks
Dysprosium oxide
Synergistic effect
Oxygen evolution
Water splitting

ABSTRACT

As the kinetically sluggish oxygen evolution reaction (OER) is considered to be a bottleneck in overall water splitting, it is necessary to develop a highly active and stable electrocatalyst to overcome this issue. Herein, we successfully fabricated a three-dimensional iron-dysprosium oxide co-regulated *in-situ* formed MOF-Ni arrays on carbon cloth (FeDy@MOF-Ni/CC) through a facile two-step hydrothermal method. Electrochemical studies demonstrate that the designed FeDy@MOF-Ni/CC catalyst requires an overpotential of only 251 mV to reach 10 mA cm^{-2} with a small Tafel slope of 52.1 mV dec^{-1}. Additionally, the stability declined by only 5.5% after 80 h of continuous testing in 1.0 M KOH. Furthermore, a cell voltage of only 1.57 V in the overall water splitting system is sufficient to achieve 10 mA cm^{-2}; this value is far better than that of most previously reported catalysts. The excellent catalytic performance originates from the unique 3D rhombus-like structure, as well as coupling synergies of Fe-Dy-Ni species. The combination of lanthanide and transition metal species in the synthesis strategy may open entirely new possibilities with promising potential in the design of highly active OER electrocatalysts.

1. Introduction

The rapid development of the global economy has increased the consumption of energy materials. It is urgent to explore alternative sustainable energy sources to reduce the dependence on fossil fuels [1,2]. Hydrogen generation by electrochemical water splitting is considered to be one of the most exciting approaches for energy storage and conversion, owing to the fact that hydrogen has a high energy density and represents a promising renewable and environmentally friendly energy resource [3–5]. In order to achieve efficient and economical water electrolysis, it is essential to prepare suitable high-activity, low-cost oxygen evolution reaction (OER) electrocatalysts. The OER is a half-reaction of water splitting and is thermodynamically unfavorable. Additionally, due to its four-electron-proton-coupled transfer process, it has a much

* Corresponding author. E-mail: xlyang@gxnu.edu.cn
# Corresponding author. E-mail: baowang@ipe.ac.cn
$ Corresponding author. E-mail: isimjant@sabic.com

This work was supported by the National Natural Science Foundation of China (21965005), Natural Science Foundation of Guangxi Province (2018GXNSFAA294077), Project of High-Level Talents of Guangxi (F-KA18015, 2018ZD004), and Innovation Project of Guangxi Graduate Education (XYCSZ2019056, YCBZ2019031).
DOI: 10.1016/S1872-2067(20)63606-3 | http://www.sciencedirect.com/science/journal/18722067 | Chin. J. Catal., Vol. 41, No. 11, November 2020

higher overpotential than the other half-reaction, the so-called hydrogen evolution reaction (HER). Therefore, the OER determines the overall efficiency of the total water splitting system [6,7]. At present, various electrocatalysts have been developed and evaluated for use in the OER. Notably, some precious metals and their oxides (IrO_2 or RuO_2) provide high OER activity and relatively low overpotential values; however, the scarcity and high costs of these metals have severely limited their large-scale application [8,9]. In contrast, the use of transition metals and their derivatives, such as Co, Ni, and Fe, is desirable owing to their low-cost and high earth-abundance [10,11].

Generally, there are two main channels to fabricate highly active OER electrocatalysts. One approach is to design catalysts with structural advantages, such as large specific surface areas, reasonable pore size, and accessible active sites; the other is to regulate the electronic environment of the reaction site to enhance the electrochemical activity [12]. The development of metal-organic frameworks (MOFs) provides new opportunities as platforms for the design of non-noble metal catalysts for water splitting, as the naturally porous structure of MOFs could promote the diffusion of the substrate or product and significantly accelerate charge transfer [13]. At the same time, the large specific surface area of MOFs exposes their active sites uniformly, making them good templates or precursors for the preparation of high-performance OER electrocatalysts [14]. However, most of the MOF systems reported at present still suffer from significant problems, including poor electrical conductivity and structurally obscured metal centers, which severely hinder their direct utilization in electrochemical processes [15].

In this regard, polymetallic electrocatalysts have been studied extensively for total water splitting [16]. For example, Hao and co-workers demonstrated trimetallic Ni_5Co_3Mo-OH nanosheets that showed high electrocatalytic performance in the OER [17]. Additionally, Guo and co-workers successfully synthesized a novel $CoSe/FeSe_2$ catalyst by taking advantage of the synergistic effects among the different components and the electron interactions between Fe, Co, and Se to enhance the OER activity [18]. Nevertheless, further breakthroughs in OER activity using transition metals remain challenging. Lanthanide ions have been used in various applications because of their strong magnetic anisotropies and large spin capacities [19]. Some research suggests that the Dy and Ni spins are ferromagnetically coupled [20]. Additionally, it could increase the magnetism of Fe and change the roughness of transition-metal-based catalyst surfaces [21,22]; however, relatively few works have focused on its OER applications.

Based on the above considerations, we first constructed a unique Fe-Dy-mediated MOF-Ni structure with exposed metal centers for the OER. The FeDy@MOF-Ni on carbon cloth (CC) catalyst was designed and fabricated through a simple two-step hydrothermal method to construct Dy_2O_3 and $FeSO_4$ doped with MOF-Ni on CC. In addition to the close contact between the MOF-Ni nanosheets and Fe-Dy, the obtained FeDy@MOF-Ni forms a 3D rhombus-like hierarchical structure in which Fe closely interacts with the adjacent Ni in the presence of Dy. As a result, the FeDy@MOF-Ni/CC exhibits impressive OER activity, with an overpotential of 251 mV at a current density of 10 mA cm^{-2}, which is on par with the performance of commercial RuO_2. When FeDy@MOF-Ni/CC is used in conjunction with CC modified with commercial Pt/C in a two-electrode system, it shows excellent activity for water splitting, requiring only 1.57 V to achieve a current density of 10 mA cm^{-2}. The unique structure of FeDy@MOF-Ni/CC creates a robust synergetic effect between Fe/Dy and the Ni active sites. It is expected to provide excellent electron transport and expose more active sites, which are responsible for the superior OER activity. These results suggest the great capacity of FeDy@MOF-Ni/CC as an efficient, economical, and durable OER electrocatalyst, demonstrating the unique electrochemical improvement in the catalyst induced by Dy-doping. Therefore, this new attractive avenue of utilizing dysprosium species to adjust the coupling effect between transition metals may provide an approach for the rational design of OER electrocatalysts.

2. Experimental

2.1. Synthesis of Ni-MOF/CC

First, CC was cut into pieces with a size of 1 cm × 1 cm. The CC was then successively sonicated in 0.5 M hydrochloric acid, deionized water, and ethanol three times, followed by drying under vacuum at 60 °C before use.

In the facile synthesis procedure, 0.58 g of $Ni(NO_3)_2·6H_2O$ and 0.05 g of CTAB were dispersed ultrasonically in 30 mL of methanol to obtain solution A. Meanwhile, 0.66 g of 2-methylimidazole was dissolved in another 30 mL of methanol to obtain solution B. Subsequently, solution A was slowly injected into solution B under continuous stirring at room temperature. After 30 min, the resulting solution and CC were transferred into a Teflon-lined stainless autoclave (90 mL) and reacted at 180 °C for 8 h. After cooling to room temperature, the MOF-Ni-modified CC was removed, washed with abundant deionized water, and vacuum-dried at 60 °C for 12 h. The obtained sample is denoted as MOF-Ni/CC.

2.2. Synthesis of FeDy@MOF-Ni/CC

For the synthesis of FeDy@MOF-Ni/CC, a facile method involving the direct mixing of $FeSO_4·7H_2O$ and Dy_2O_3 in a 3:2 molar ratio was designed. First, 0.18 mmol Dy_2O_3 and 0.27 mmol $FeSO_4·7H_2O$ were dissolved into 10 mL deionized water and 10 mL ethanol. After stirring for 1.0 h, 3 mL of hydrazine hydrate was gradually added to the above solution. Ten minutes later, the resulting mixture and the as-prepared MOF-Ni/CC were transferred into a Teflon-lined stainless autoclave (50 mL) and reacted at 180 °C for 20 h. After cooling to room temperature, the black sample was removed, thoroughly washed with deionized water, and vacuum-dried at 60 °C for 3.0 h. The obtained sample was named FeDy@MOF-Ni/CC.

2.3. Synthesis of Dy@MOF-Ni/CC, Fe@MOF-Ni/CC, and DyFe/CC

The preparation process for Dy@MOF-Ni/CC, Fe@MOF-Ni/CC, and DyFe/CC was similar to that of FeDy@MOF-Ni, except that only 0.18 mmol Dy_2O_3 or 0.27 mmol $FeSO_4·7H_2O$ were used for the preparation of Dy@MOF-Ni or Fe@MOF-Ni, respectively. For comparison, Fe-Dy/CC was also prepared using pure CC instead of MOF-Ni/CC using the approach described above.

2.4. Synthesis of $Ni(OH)_2$/CC and FeDy@$Ni(OH)_2$/CC

The preparation process was similar to that of MOF-Ni. Specifically, 0.58 g of $Ni(NO_3)_2·6H_2O$ and 0.05 g of CTAB were dispersed ultrasonically in 30 mL of methanol. The resulting solution and CC were then transferred into a Teflon-lined stainless autoclave (50 mL) and reacted at 180 °C for 8 h. The resulting product was named $Ni(OH)_2$/CC. Subsequently, the $Ni(OH)_2$/CC and a solution containing $FeSO_4·7H_2O$ and Dy_2O_3 were transferred into a Teflon-lined stainless autoclave (50 mL) and reacted at 180 °C for 20 h, as discussed above. The resulting composite was called FeDy@$Ni(OH)_2$/CC.

2.5. Electrochemical measurements

Electrochemical measurements were carried out in a standard three-electrode system operated using a VMP3B-2x2 electrochemical analyzer (CH Instruments, Inc, France). The catalysts loaded on the CC were used as the working electrode (1 cm × 1 cm), a saturated calomel electrode (SCE) was used as the reference electrode, and a Pt foil was used as the counter electrode. Electrochemical measurements of the catalysts were conducted in 1.0 M KOH solution. Polarization curves were acquired using linear sweep voltammetry (LSV) at a scan rate of 5 mV s^{-1}. Electrochemical impedance spectroscopy (EIS) measurements were carried out in the frequency range of 200 kHz–0.1 Hz. Chronopotentiometry was utilized for long-term stability tests. All measured potentials were calibrated to the RHE using the following equation: E(RHE) = E(SCE) + 0.2415 V + 0.059·pH (Fig. S1). All electrochemical data were corrected against ohm potential drop. CV tests of the catalysts were conducted at various scan rates in 1 M KOH solution to obtain the electrochemical double-layer capacitance (C_{dl}).

3. Results and discussion

3.1. Analysis of the synthetic strategy

A schematic diagram of the fabrication process of FeDy@MOF-Ni/CC using the facile two-step hydrothermal strategy is illustrated in Fig. 1a. First, a piece of clean CC was immersed in a methanol solution containing $Ni(NO_3)_2$, 2-methylimidazole, and CTAB, and then hydrothermally heated to 180 °C for 8 h in a Teflon-lined stainless autoclave. A series of MOF-Ni-coated CC composites were prepared, and referred to as MOF-Ni/CC. Subsequently, the obtained MOF-Ni/CC composites were immersed in a mixed solution of $FeSO_4$, Dy_2O_3, and hydrazine. The resulting mixture was hydrothermally heated to 180 °C to acquire the final product, Fe-Dy-oxide-modulated MOF-Ni/CC. Unless otherwise specified, this is abbreviated as FeDy@MOF-Ni in the following discussion.

3.2. Crystallinity and microstructural analyses

X-ray diffraction (XRD) patterns were obtained and used to analyze the phase composition of the materials. As shown in Fig. S2a, the crystal structure of MOF-Ni gave rise to six strong diffraction peaks, which is consistent with previous reports for MOF-Ni [23]. In addition, the XRD patterns of FeDy@MOF-Ni, together with those of Fe@MOF-Ni and Dy@MOF-Ni, are shown in Fig. 1b and Fig. S2b. The XRD data of FeDy@MOF-Ni, Fe@MOF-Ni, and Dy@MOF-Ni match well with the diffraction peaks of Dy_2O_3 (JCPDS: 43-1006) [24,25] and Fe_2O_3 (JCPDS: 39-1346). The crystal structure of MOF-Ni was gradually destroyed during the FeDy@MOF-Ni synthesis due to ion exchange resulting in structural deformation [26,27].

The microstructures of the catalysts were examined using scanning electron microscopy (SEM) and transmission electron

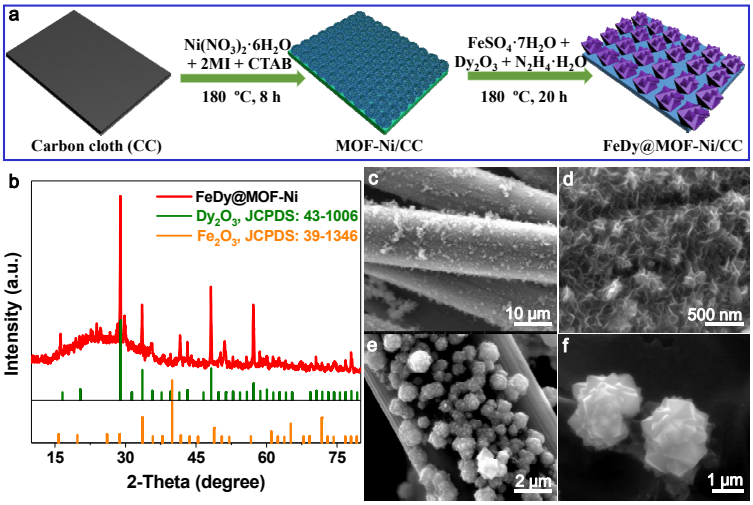

Fig. 1. (a) Schematic illustration of the synthesis process for FeDy@MOF-Ni; (b) XRD patterns of contrast catalyst; SEM images of (c,d) MOF-Ni, (e,f) FeDy@MOF-Ni.

microscopy (TEM). The SEM image in Fig. 1c shows that MOF-Ni was successfully grafted onto the CC surface, and the high-resolution SEM image in Fig. 1d displays a lamellar structure composed of two-dimensional nanosheets. However, after treatment with the Fe-Dy precursor, the morphologies of the synthesized products underwent dramatic changes, from uniformly distributed lamellar structures to irregular rhombus-like structures (Figs. 1e-f). The changes in their morphologies may have been due to the formation process, namely, dissolution-regrowth during the construction of the final material. To explore the dissolution-regrowth mechanism, we investigated the thermal stability of the as-prepared MOF-Ni/CC and monitored it via SEM. The SEM image (Fig. S3) shows that the MOF-Ni was completely dissociated after 20 h at 180 °C in water/methanol mixture. On the other hand, FeDy@MOF-Ni was formed under the same conditions. These results indicated that the ion displacement occurs simultaneously with MOF-Ni dissociation to create a relatively stable nanocomposite on the surface of the CC. In addition, elemental analysis (Table S1) indicated great changes in the element N before and after the hydrothermal treatment of MOF-Ni, further confirming the dissolution-regrowth mechanism.

The rhombus-like structure of FeDy@MOF-Ni was further investigated using TEM (Fig. 2a). It can be observed that the composite is a bulk material composed of many stacked lamellar layers. This unique structure was believed to facilitate the transport of electrolytes and gas emissions. The high-resolution TEM image shows that FeDy@MOF-Ni exhibits two distinct types of lattice fringes with spacings of 0.31 and 0.37 nm, respectively, corresponding to the (222) plane of Dy_2O_3 and the (210) plane of Fe_2O_3 (Fig. 2b). In addition, the HAADF-STEM image of FeDy@MOF-Ni demonstrates that the elements Ni, Dy, Fe, C, O, and N were uniformly distributed throughout the structure (Fig. 2c).

3.3. Surface characteristics and porosity analysis

The surface functional groups of the synthesized materials were investigated using Fourier-transform infrared spectroscopy (FTIR). As shown in Fig. 3a, FeDy@MOF-Ni exhibits three

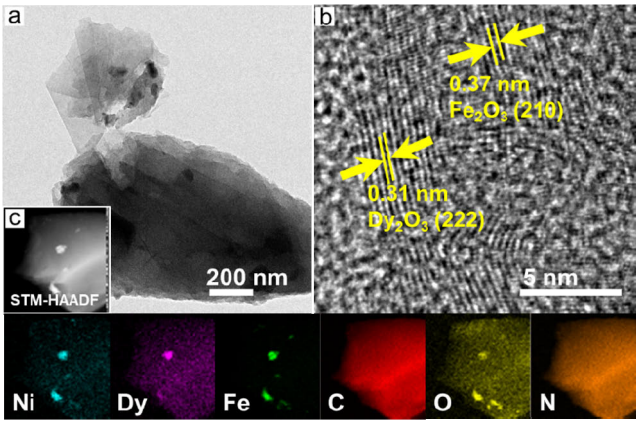

Fig. 2. (a) TEM and (b) high-resolution TEM images of FeDy@MOF-Ni. (c) HAADF-STEM image of FeDy@MOF-Ni and the corresponding elemental mappings of Ni, Dy, Fe, C, O, and N in the composite.

characteristic peaks typical of FeDy@MOF-Ni and Dy@MOF-Ni, where the two peaks at *ca*. 550 and 726 cm^{-1} are the stretching vibrations of Dy–O [28,29], and the peak at *ca*. 3609 cm^{-1} can be ascribed to the stretching vibration of Dy–OH. The FTIR spectra of Fe@MOF-Ni reveals three characteristic peaks at 1623, 3160, and 3247 cm^{-1}, which correspond to the stretching vibrations of adsorbed H_2O and of O–H and N–H in the imidazole functional groups, respectively [30-31], implying the presence of the MOF-Ni structure in the composite. Raman spectroscopy was applied to further verify the formation of FeDy@MOF-Ni. As shown in Fig. 3b, the Raman spectrum of FeDy@MOF-Ni also corresponds to those of Dy@MOF-Ni and Fe@MOF-Ni; the three bands at 314, 397, and 501 cm^{-1} were assigned to Dy–O vibration [32] and that at 1065 cm^{-1} was attributed to Ni–O vibration [33]. More importantly, the additional Raman characteristic bands centered at 603 and 662 cm^{-1} clearly confirmed the existence of partial Fe_2O_3 species in the composite [34–36]. All the above phenomena indicated that the engineering of the FeDy@MOF-Ni sample was successfully actualized using a simple two-step hydrothermal reaction.

Thermogravimetric analysis (TGA) was used to explore the mass variation during the pyrolysis of FeDy@MOF-Ni, Fe@MOF-Ni, and Dy@MOF-Ni in an O_2 atmosphere in the temperature range of 25 °C to 800 °C with a heating rate of 10 °C min^{-1} (Fig. 3c and Fig. S4). In Fig. 3c, the mass loss at temperatures below 230 °C was primarily due to the evaporation of adsorbed water [37,38]. The sharp exothermic peak indicates that the MOF appears to be pyrolyzed when the temperature reaches approximately 263.8 °C [39]. At higher temperatures near 836.1 °C, a slight weight loss occurs due to continuous crystallization and catalyst aggregation [40]. Interestingly, no mass loss is observed at such high temperatures for the Dy@MOF-Ni material, while a weight loss appears at 379.3 °C due to the dehydration of the Dy metal hydroxides [13,32]. Moreover, the mass loss of FeDy@MOF-Ni was 16.2%, which was much lower than that of Fe@MOF-Ni (47.4%), but higher than that of Dy@MOF-Ni (5.2%) in a similar temperature range (Fig. S3). This noticeable difference proved once again that the Dy and Fe species had been successfully doped into the MOF-Ni.

The Brunauer-Emmett-Teller (BET) gas-sorption measurements demonstrated that the FeDy@MOF-Ni material showed the characteristics of a type III isotherm with a pore size range of 30–50 nm and a corresponding BET specific surface area of approximately 19.3 $m^2\ g^{-1}$ (Fig. 3d). However, the relative BET particular surface area of the Ni-MOF was approximately 229.0 $m^2\ g^{-1}$, further indicating the dissociation of the Ni-MOF precursor and the successful preparation of FeDy@MOF-Ni. Although its BET value was smaller than that of Ni-MOF, FeDy@MOF-Ni exhibited excellent OER performance due to the strong synergistic effects between the three metals and as a result of its high-valence Ni^{3+} and Fe^{3+} active sites.

3.4. XPS analysis

The compositions and surface chemical states of the as-prepared catalysts were further characterized using X-ray

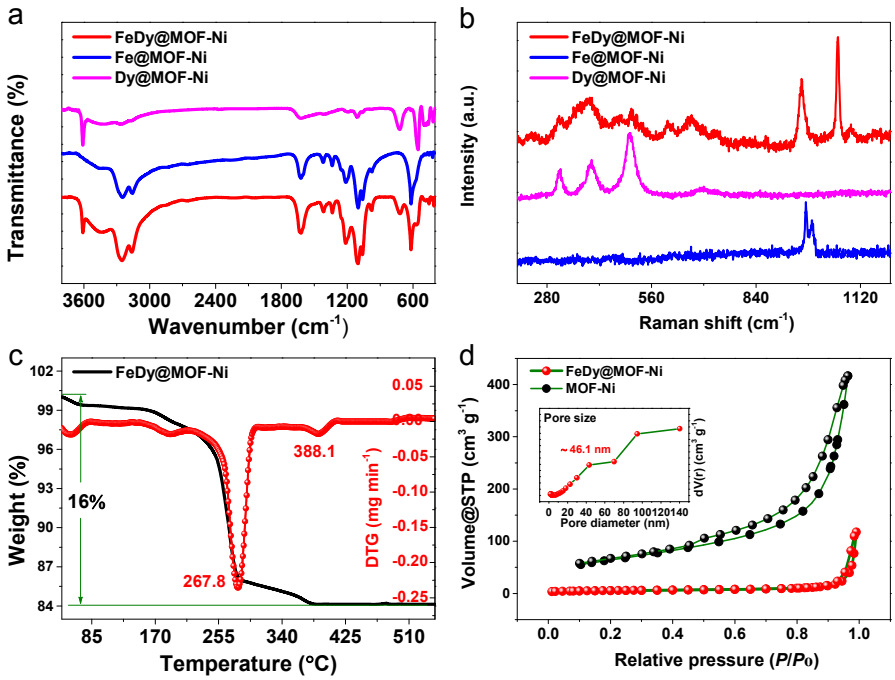

Fig. 3. (a) Fourier-transform infrared spectra and (b) Raman spectra of the FeDy@MOF-Ni, Fe@MOF-Ni, and Dy@MOF-Ni catalysts. (c) Thermal gravimetric (TG) analysis and derivative thermal gravimetry (DTG) curves of FeDy@MOF-Ni obtained in an O_2 atmosphere at a heating rate of 2.5 °C min^{-1}. (d) N_2 adsorption-desorption isotherms and the pore size distribution curves obtained using the BJH method (inset) for Ni-MOF and FeDy@MOF-Ni.

photoelectron spectroscopy (XPS). The survey spectrum (Fig. S5a) reveals the presence of C, N, O, Ni, Fe, and Dy in the composite; the high-resolution C 1*s* spectrum was referenced to C=O (284.0 eV), C–C (284.8 eV), and C–O (286.0 eV) as calibration standards (Fig. S5b) [41]. Meanwhile, for the MOF-Ni precursor, the ratio of Ni^{2+}/Ni^{3+} in the high-resolution Ni 2*p* region was 2.0 (Fig. S5c). Only pyridinic-N (398.5 eV) and pyrrolic-N (399.9 eV) were observed in the high-resolution N 1*s* spectrum (Fig. S5d) [42,43], which was consistent with the theoretical results.

The high-resolution Ni 2*p* spectrum of the as-prepared catalysts exhibits characteristic Ni $2p_{3/2}$ and Ni $2p_{1/2}$ peaks as well as the corresponding shake-up satellites, with the peaks at 855.1 and 872.8 eV being associated with the Ni^{2+} species, while those at 856.6 and 873.7 eV are associated with Ni^{3+} species (Fig. 4a) [44,45]. In addition, the other pairs of peaks were assigned as satellite peaks. It is worth noting that the high-resolution Ni 2*p* spectrum of Dy@MOF-Ni shows a Ni^0 peak, because Ni^{2+} is more easily reduced than Dy^{3+} ($Ni^{2+} + 2e^- \rightarrow Ni$, $\varphi^\Theta = -0.23$ V; $Dy^{3+} + 3e^- \rightarrow Dy$, $\varphi^\Theta = -2.295$ V). However, the metallic Ni species in FeDy@MOF-Ni and Fe@MOF-Ni are hard to detect because Fe species has a higher standard redox potential Fe^{3+}/Fe^{2+} ($\varphi^\Theta = +0.77$) than Ni^{2+}/Ni^0 ($\varphi^\Theta = -0.23$ V), thereby oxidizing the Ni^0 species. Interestingly, the Ni^{2+}/Ni^{3+} ratios decrease when both Fe and Dy species are added, with FeDy@MOF-Ni having significantly lower values than

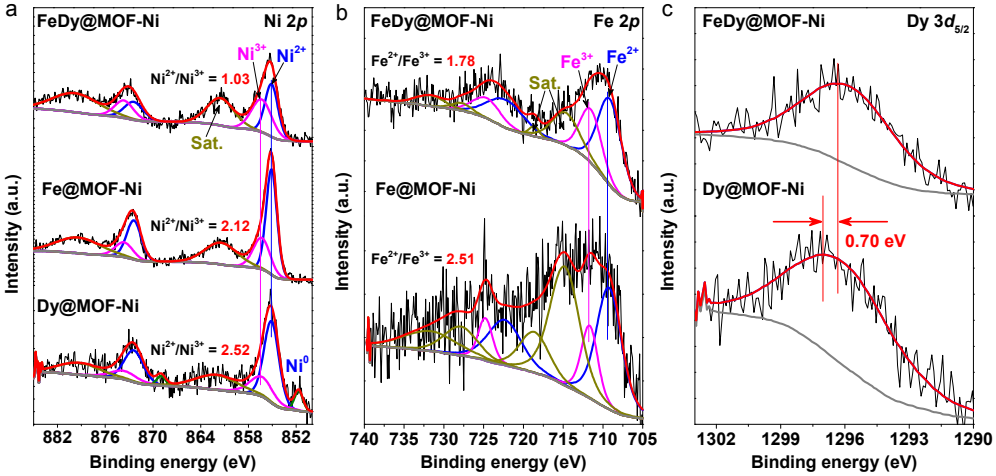

Fig. 4. High-resolution XPS profiles of the (a) Ni 2*p*, (b) Fe 2*p*, and (c) Dy 3*d* levels of FeDy@MOF-Ni, Fe@MOF-Ni, and Dy@MOF-Ni.

Fe@MOF-Ni (2.12), Dy@MOF-Ni (2.52), and MOF-Ni (2.0), suggesting a strong coupling effect for FeDy@MOF-Ni during the hydrothermal reactions.

At the same time, the Fe species of the various catalysts were also explored (Fig. 4b). A series of peaks can be fitted in the high-resolution Fe 2*p* XPS profiles, of which those with binding energies at approximately 709.9 eV and 711.7 eV are assignable to Fe^{2+} and Fe^{3+}, respectively [46]. The Fe^{2+}/Fe^{3+} ratio of FeDy@MOF-Ni was lower than that of Fe@MOF-Ni, implying that Fe^{2+} can be converted to a higher valence state in the presence of Dy species. In the high-resolution Dy $3d_{5/2}$ spectrum of FeDy@MOF-Ni in Fig. 4c, a peak corresponding to Dy_2O_3 was fitted at 1297.0 eV [47,48]; this peak was shifted 0.70 eV toward lower binding energy compared with that of Dy@MOF-Ni, which could be due to the effect of the surface enrichment of Ni and Fe species on the charge density around the Dy species. These results indicate that the content of high-valence Ni and Fe species was remarkably improved in FeDy@MOF-Ni by the participation of Dy species. The positive effects of high-valent transition metal species on OER performance have been widely reported in the literature [49–50]. Additionally, inductively coupled plasma spectrometry (ICP) indicated the Ni/Fe ratio of FeDy@MOF-Ni was approximately 1:1 (Table S2).

3.5. Electrocatalytic performance analysis

The electrocatalytic activity of all the OER catalysts was evaluated using linear sweep voltammetry (LSV) at a scan rate of 5 mV s^{-1} in 1.0 M KOH solution. All the LSV polarization curves were processed using iR compensation (Fig. S6) and RHE correction due to the effect of ohmic resistance. Furthermore, FeDy@MOF-Ni showed the lowest ohmic resistance, suggesting that it had the highest conductivity among the catalysts. For comparison, the OER performance of the catalyst RuO_2 (Aladdin Industrial Corporation, 2.0 mg cm^{-2} loading on CC) was also measured. The CV curves overlapped after 3–5 cycles in all the measurements. As shown in the polarization curves in Fig. 5a, a pair of sharp Ni^{2+}/Ni^{3+} redox peaks appeared in the overpotential range of 0.1 to 0.2 V, which were ascribed to the formation of NiOOH species [2]. Notably, FeDy@MOF-Ni displays superior catalytic activity (overpotential of 251 mV) at a current density of 10 mA cm^{-2}; this overpotential was much smaller than those of Fe@MOF-Ni (288 mV), Dy@MOF-Ni (382 mV), MOF-Ni (361 mV), and Fe-Dy (401 mV), and on par with that of commercial RuO_2 (253 mV). The corresponding Tafel plots are a critical parameter to estimate OER reaction kinetics. In Fig. 5b, the plot of FeDy@MOF-Ni is presented. Its Tafel slope of 51.8 mV dec^{-1} is much lower than those of Fe@MOF-Ni (54.6 mV dec^{-1}), Dy@MOF-Ni (105.1 mV dec^{-1}), MOF-Ni (96.9 mV dec^{-1}), Fe-Dy (80.8 mV dec^{-1}), and RuO_2 (62.6 mV dec^{-1}). This merit indicates that dysprosium could optimize the coupling effect between transition metals to enhance OER performance. The OER activity of FeDy@MOF-Ni was further highlighted by comparing our best catalyst to other reported high-performance polymetallic catalysts reported in alkaline media (Fig. 5c) [51–55].

In order to further determine the intrinsic OER activities of the catalysts, their turnover frequency (TOF) values were calculated using the formula below:

$$\mathrm{TOF} = \frac{J * A}{4 * F * n}$$

Where *J* corresponds to the current density, *A* is the area of the electrode with the number of moles of the catalysts, *F* is the Faraday constant (96,485 C mol^{-1}) and *n* is the number of moles of all metal atoms. Note that all the metal atoms were assumed to be active species [56]. As shown in Fig. 5d, FeDy@MOF-Ni exhibited a high TOF value of 22.9 s^{-1} at 300 mV, which was higher than those of Fe@MOF-Ni (6.61 s^{-1}), and Dy@MOF-Ni (0.71 s^{-1}), indicating the superior OER activity of FeDy@MOF-Ni compared to the other catalysts.

In addition to the TOF value, the electrochemical active surface area (EASA) is another parameter that indirectly indicates OER activity. In general, the higher the double-layer capaci-

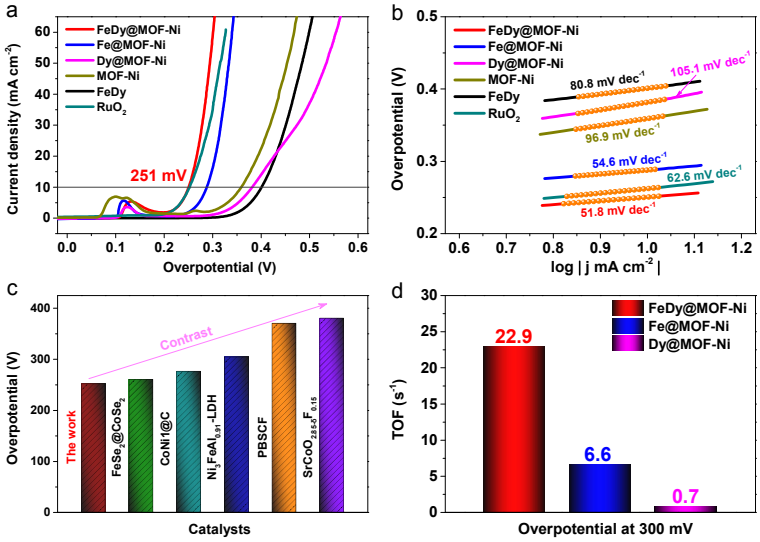

Fig. 5. OER performance of the different catalysts in 1.0 M KOH. (a) LSV curves obtained at a scan rate of 5 mV s^{-1}. (b) Tafel slopes calculated from the LSV curves. (c) Comparison with the overpotentials of recently reported catalysts at 10 mA cm^{-2}. (d) Comparison of the TOF of FeDy@MOF-Ni, Fe@MOF-Ni, and Dy@MOF-Ni at an overpotential of 300 mV.

tance (C_{dl}), the smaller the overpotential will be at a given current density. The EASA is proportional to the C_{dl}, which can be acquired from CV curves obtained at different scan rates in a non-faradaic potential region [57,58]. As shown in Fig. S7, the C_{dl} of FeDy@MOF-Ni was obtained from cyclic voltammogram curves (CVs) at scan rates of 100, 120, 140, 160, 180, and 200 mV s^{-1}. The results show that the catalyst FeDy@MOF-Ni had a C_{dl} of 0.71 mF cm^{-2}, which was higher than those of Fe@MOF-Ni (0.55 mF cm^{-2}), Dy@MOF-Ni (0.68 mF cm^{-2}), and Fe-Dy (0.56 mF cm^{-2}) (Fig. S8).

There are several benefits to the use of MOF-Ni as a nickel precursor. Firstly, it can improve chemical absorption through the hydroxyl group on the catalyst surface due to the stronger OH–Ni bond [49]. Secondly, its unique 2D-structured nanosheets expose an abundance of coordinatively unsaturated metal sites and structural defects [59,60]. Finally, its OER performance can be significantly improved by doping it with other metal species [61,62]. Therefore, although the MOF-Ni and $Ni(OH)_2$ precursors have similar lamellar structures (Figs. S9,10), the OER performance of FeDy@MOF-Ni is far superior to that of the catalyst FeDy@$Ni(OH)_2$ under the same conditions. This result implies the significant role of the MOF-Ni precursor in the overall process.

To investigate the OER performance for potential industrial applications, the overall water splitting reaction was explored under industrially relevant conditions using a two-electrode configuration. FeDy@MOF-Ni was used as the anodic oxygen-generating catalyst, and CC modified with commercial Pt/C modified was used as the cathodic hydrogen-producing catalyst in 1.0 M KOH electrolyte (Fig. 6a). As we expected, FeDy@MOF-Ni exhibited excellent catalytic performance, affording a current density of 10 mA cm^{-2} at a cell voltage of only 1.57 V. Furthermore, the stability of FeDy@MOF-Ni was measured in a three-electrode system, and the overpotential increased only 7 mV at a current of 10 mA cm^{-2} current after 80 h (Fig. 6b). The SEM images and XPS data for FeDy@MOF-Ni after

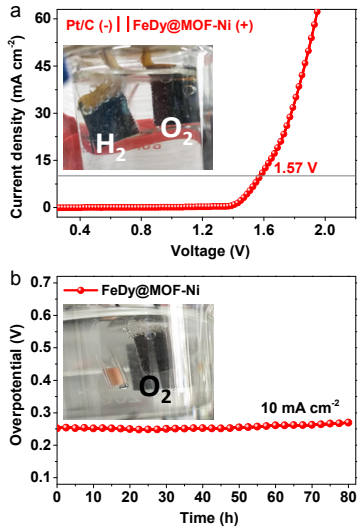

Fig. 6. (a) Overall water splitting using FeDy@MOF-Ni and commercial Pt/C on a CC surface in a two-electrode system. (b) Long-term stability test of the catalyst FeDy@MOF-Ni; the system was operated continuously at 10 mA cm^{-2} for 80 h.

the long-term stability test showed that it had retained its irregular morphology and richness in Fe^{3+} and Ni^{3+} species (Figs. S11,12). These results demonstrated that FeDy@MOF-Ni has excellent mass transport (inward movement of OH^- and outward diffusion of oxygen gas) as well as high electrical conductivity.

4. Conclusions

In summary, a unique FeDy@MOF-Ni-CC composite with a hierarchical rhombus-like structure was fabricated using a two-step approach followed by a hydrothermal method. The catalytic results indicate that the optimum catalyst FeDy@MOF-Ni-CC has an excellent OER activity and requires an overpotential of only 251 mV to drive a current density of 10 mA cm^{-2}. Moreover, the catalyst also exhibits a small Tafel slope of ~52 mV dec^{-1} as well as reasonable stability in 1.0 M KOH. The high OER performance is mainly due to the 3D rhombus-like structure, which induces high electrical conductivity, and the synergies between the multiple metal centers. This work provides an alternative for the design and fabrication of low-cost, highly efficient, and robust anodic catalysts by introducing dysprosium to regulate the effects of transition metals.

Appendix A. Supplementary data

Figs. S1–S12 and Tables S1–3 give more details on characterization of our synthesized materials and their catalytic performance data; additional photograph, XRD, SEM, XPS and catalytic performance data (PDF).

References

[1] Y. Guo, J. Tang, Z. Wang, Y. Sugahara, Y. Yamauchi, *Small*, **2018**, 14, 1802442.
[2] R. Xiang, C. Tong, Y. Wang, L. Peng, Y. Nie, L. Li, X. Huang, Z. Wei, *Chin. J. Catal.*, **2018**, 39, 1736–1745.
[3] Z. Chen, H. Xu, Y. Ha, X. Li, M. Liu, R. Wu, *Appl. Catal. B*, **2019**, 250, 213–223.
[4] G. Chen, J. Du, X. Wang, X. Shi, Z. Wang, H.-P. Liang, *Chin. J. Catal.*, **2019**, 40, 1540–1547.
[5] H. Gong, Y. Zhang, Y. Cao, M. Luo, Z. Feng, W. Yang, K. Liu, H. Cao, H. Yan, *Appl. Catal. B*, **2018**, 237, 309–317.
[6] Z.-M. Luo, J.-W. Wang, J.-B. Tan, Z.-M. Zhang, T.-B. Lu, *ACS Appl. Mater. Interfaces*, **2018**, 10, 8231–8237.
[7] D. Lyu, Y. B. Mollamahale, S. Huang, P. Zhu, X. Zhang, Y. Du, S. Wang, M. Qing, Z. Q. Tian, P. K. Shen, *J. Catal.*, **2018**, 368, 279–290.
[8] S. Xie, F. Li, S. Xu, J. Li, W. Zeng, *Chin. J. Catal.*, **2019**, 40, 1205–1211.
[9] J. Xing, F. Lin, L. Huang, Y. Si, Y. Wang, L. Jiao, *Chin. J. Catal.*, **2019**, 40, 1352–1359.
[10] S. Sun, Y. Sun, Y. Zhou, S. Xi, X. Ren, B. Huang, H. Liao, L. P. Wang, Y. Du, Z. J. Xu, *Angew. Chem. Int. Ed.*, **2019**, 58, 6042–6047.
[11] L. Huang, Y. Zou, D. Chen, S. Wang, *Chin. J. Catal.*, **2019**, 40, 1822–1840.
[12] Y. Zhou, H. C. Zeng, *Small*, **2018**, 14, e1704403.
[13] B. Devi, R. Rani Koner, A. Halder, *New J. Chem.*, **2017**, 41, 7972–7979.

Graphical Abstract

Chin. J. Catal., 2020, 41: 1745–1753 doi: 10.1016/S1872-2067(20)63606-3

Dissolution-regrowth of hierarchical Fe-Dy oxide modulates the electronic structure of nickel-organic frameworks as highly active and stable water splitting electrocatalysts

Zixia Wan, Qiuting He, Jundan Chen, Tayirjan Taylor Isimjan *, Bao Wang *, Xiulin Yang *
Guangxi Normal University

Hierarchical Fe-Dy oxide co-regulated MOF-Ni on carbon cloth was fabricated by a facile two-step hydrothermal method. The resulting catalyst exhibited highly active and stable oxygen evolution for the overall water splitting reaction in alkaline media.

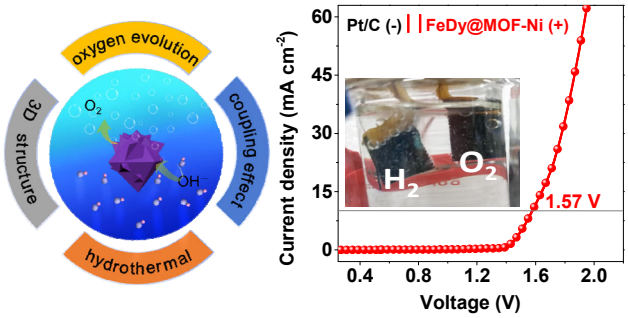

[14] Z. Chen, Y. Ha, H. Jia, X. Yan, M. Chen, M. Liu, R. Wu, *Adv. Energy Mater.*, **2019**, 9, 1803918.
[15] W. Q. Zaman, W. Sun, M. Tariq, Z. Zhou, U. Farooq, Z. Abbas, L. Cao, J. Yang, *Appl. Catal. B*, **2018**, 244, 295–302.
[16] Y.-T. Liu, X.-D. Zhu, Y. Xie, *J. Mater. Chem. A*, **2018**, 6, 21255–21260.
[17] S. Hao, L. Chen, C. Yu, B. Yang, Z. Li, Y. Hou, L. Lei, X. Zhang, *ACS Energy Lett.*, **2019**, 4, 952–959.
[18] K. Guo, Z. Zou, J. Du, Y. Zhao, B. Zhou, C. Xu, *Chem. Commun.*, **2018**, 54, 11140–11143.
[19] G. Castro, M. Regueiro-Figueroa, D. Esteban-Gómez, P. Pérez-Lourido, C. Platas-Iglesias, L. Valencia, *Inorg. Chem.*, **2016**, 55, 3490–3497.
[20] A. Okazawa, T. Nogami, H. Nojiri, T. Ishida, *Inorg. Chem.*, **2008**, 47, 9763–9765.
[21] X. T. Tang, Z. W. Lu, A. Z. Sun, *J. Magn. Magn. Mater.*, **2019**, 475, 10–13.
[22] C. Li, A. Sun, Z. Tian, X. Zhang, B. Ma, *J. Magn. Magn. Mater.*, **2018**, 462, 41–45.
[23] Y. Hou, W. Hu, X. Zhou, Z. Gui, Y. Hu, *Ind. Eng. Chem. Res.*, **2017**, 56, 8778–8786.
[24] A. W. Xu, Y. P. Fang, L. P. You, H. Q. Liu, *J. Am. Chem. Soc.*, **2003**, 125, 1494–1495.
[25] K. Ojha, E. M. Farber, T. Y. Burshtein, D. Eisenberg, *Angew. Chem. Int. Ed.*, **2018**, 57, 17168–17172.
[26] Y. Ye, F. Cai, H. Li, H. Wu, G. Wang, Y. Li, S. Miao, S. Xie, R. Si, J. Wang, X. Bao, *Nano Energy*, **2017**, 38, 281–289.
[27] X. Wang, H. Xiao, A. Li, Z. Li, S. Liu, Q. Zhang, Y. Gong, L. Zheng, Y. Zhu, C. Chen, D. Wang, Q. Peng, L. Gu, X. Han, J. Li, Y. Li, *J. Am. Chem. Soc.*, **2018**, 140, 15336–15341.
[28] S. Zinatloo-Ajabshir, M. S. Morassaei, M. Salavati-Niasari, *J. Clean. Prod.*, **2019**, 222, 103–110.
[29] A. Salehabadi, M. Salavati-Niasari, M. Ghiyasiyan-Arani, *J. Alloys Compd.*, **2018**, 745, 789–797.
[30] M. A. R. Anjum, M. H. Lee, J. S. Lee, *ACS Catal.*, **2018**, 8, 8296–8305.
[31] R. Boppella, W. Yang, J. Tan, H.-C. Kwon, J. Park, J. Moon, *Appl. Catal. B*, **2019**, 242, 422–430.
[32] J.-G. Kang, J. Seog Gwag, Y. Sohn, *Ceram. Int.*, **2015**, 41, 3999–4006.
[33] Z.-J. Chen, G.-X. Cao, L.-Y. Gan, H. Dai, N. Xu, M.-J. Zang, H.-B. Dai, H. Wu, P. Wang, *ACS Catal.*, **2018**, 8, 8866–8872.
[34] I. S. Molchan, G. E. Thompson, R. Lindsay, P. Skeldon, V. Likodimos, G. E. Romanos, P. Falaras, G. Adamova, B. Iliev, T. J. S. Schubert, *RSC Adv.*, **2014**, 4, 5300–5311.
[35] S. Rehman, W. Yang, F. Liu, Y. Hong, T. Wang, Y. Hou, *Inorg. Chem. Front.*, **2015**, 2, 576–583.
[36] R. Kant, D. Kumar, V. Dutta, *RSC Adv.*, **2015**, 5, 52945–52951.
[37] X. Yang, X. Wang, Y. Feng, G. Zhang, T. Wang, W. Song, C. Shu, L. Jiang, C. Wang, *J. Mater. Chem. A*, **2013**, 1, 473–477.
[38] X. Peng, F. Gao, J. Zhao, J. Li, J. Y. Qu, H. Fan, *J. Mater. Chem. A*, **2018**, 6, 20861–20868.
[39] F. Yang, P. Song, X. Liu, B. Mei, W. Xing, Z. Jiang, L. Gu, W. Xu, *Angew. Chem. Int. Ed.*, **2018**, 57, 12303–12307.
[40] S. Jiang, K. Ithisuphalap, X. Zeng, G. Wu, H. Yang, *J. Power Sources*, **2018**, 399, 66–75.
[41] J. Guo, B. Wang, D. Yang, Z. Wan, P. Yan, J. Tian, T. T. Isimjan, X. Yang, *Appl. Catal. B*, **2020**, 265, 118584.
[42] S. H. Ahn, X. Yu, A. Manthiram, *Adv. Mater.*, **2017**, 29, 1606534.
[43] G. Ye, K. Zhao, Z. He, R. Huang, Y. Liu, S. Liu, *ACS Sustainable Chem. Eng.*, **2018**, 6, 15624–15633.
[44] Y. Fu, H.-Y. Yu, C. Jiang, T.-H. Zhang, R. Zhan, X. Li, J.-F. Li, J.-H. Tian, R. Yang, *Adv. Funct. Mater.*, **2018**, 28, 1705094.
[45] Y. Hou, M. Qiu, M. G. Kim, P. Liu, G. Nam, T. Zhang, X. Zhuang, B. Yang, J. Cho, M. Chen, C. Yuan, L. Lei, X. Feng, *Nat. Commun.*, **2019**, 10, 1392.
[46] X. Guo, X. Jia, P. Song, J. Liu, E. Li, M. Ruan, W. Xu, *J. Mater. Chem. A*, **2017**, 5, 17470–17475.
[47] A. V. Fetisov, G. A. Kozhina, S. K. Estemirova, V. B. Fetisov, R. I. Gulyaeva, *Phys. C*, **2015**, 508, 62–68.
[48] M. Matsumiya, Nucleation Behaviors of Nd and Dy in TFSA-Based Ionic Liquids, in: M. Aliofkhazraei (ed.), *Electroplating of Nanostructures*, **2015**, DOI 10.5772/61292.
[49] H. Meng, Z. Ren, S. Du, J. Wu, X. Yang, Y. Xue, H. Fu, *Nanoscale*, **2018**, 10, 10971–10978.
[50] F. Zhou, H. N. Tien, W. L. Xu, J. T. Chen, Q. Liu, E. Hicks, M. Fathizadeh, S. Li, M. Yu, *Nat. Commun.*, **2017**, 8, 2107.
[51] H. Liu, Y. Wang, X. Lu, Y. Hu, G. Zhu, R. Chen, L. Ma, H. Zhu, Z. Tie, J. Liu, Z. Jin, *Nano Energy*, **2017**, 35, 350–357.
[52] Y. Zhu, L. Zhang, B. Zhao, H. Chen, X. Liu, R. Zhao, X. Wang, J. Liu, Y. Chen, M. Liu, *Adv. Funct. Mater.*, **2019**, 29, 1901783.
[53] G. Zhu, X. Xie, X. Li, Y. Liu, X. Shen, K. Xu, S. Chen, *ACS Appl. Mater. Interfaces*, **2018**, 10, 19258–19270.
[54] W. Wang, Y. Yang, D. Huan, L. Wang, N. Shi, Y. Xie, C. Xia, R. Peng, Y. Lu, *J. Mater. Chem. A*, **2019**, 7, 12538–12546.
[55] X. Zhang, J. Luo, K. Wan, D. Plessers, B. Sels, J. Song, L. Chen, T. Zhang, P. Tang, J. R. Morante, J. Arbiol, J. Fransaer, *J. Mater. Chem. A*, **2019**, 7, 1616–1628.
[56] N. Xu, Y. Zhang, T. Zhang, Y. Liu, J. Qiao, *Nano Energy*, **2019**, 57, 176–185.
[57] K. Zhang, S. Deng, Y. Zhong, Y. Wang, J. Wu, X. Wang, X. Xia, J. Tu,

Chin. J. Catal., **2019**, 40, 1063–1069.
[58] X. Li, W. Xue, R. Mo, S. Yang, H. Li, J. Zhong, *Chin. J. Catal.*, **2019**, 40, 1576–1584.
[59] G. Hai, X. Jia, K. Zhang, X. Liu, Z. Wu, G. Wang, *Nano Energy*, **2017**, 44, 345–352.
[60] X. Wang, H. Zhang, Z. Yang, C. Zhang, S. Liu, *Ultrason. Sonochem.*, **2019**, 59, 104714.
[61] F. S. Zhang, J. W. Wang, J. Luo, R. R. Liu, Z. M. Zhang, C. T. He, T. B. Lu, *Chem. Sci.*, **2018**, 9, 1375–1384.
[62] G. Dong, M. Fang, J. Zhang, R. Wei, L. Shu, X. Liang, S. Yip, F. Wang, L. Guan, Z. Zheng, J. C. Ho, *J. Mater. Chem. A*, **2017**, 5, 11009–11015.

溶解-再生长法构建Fe-Dy氧化物调控镍-有机框架电子结构的高性能水分解电催化剂

万梓霞[a], 何秋婷[a], 陈菊丹[a], 泰勒·伊西姆扬[c,$], 王 宝[b,#], 杨秀林[a,*]
[a]广西师范大学化学与药学学院广西低碳能源材料重点实验室, 广西桂林541004, 中国
[b]中国科学院过程工程研究所生化工程国家重点实验室, 北京100190, 中国
[c]阿卜杜拉国王科技大学的沙特阿拉伯基础工业公司, 图瓦勒23955-6900, 沙特阿拉伯

摘要: 世界经济的快速发展加剧了能源消耗, 迫切需要探索替代的可持续能源, 以减少对化石燃料的依赖. 电化学水分解制氢由于具有较高的能量密度, 是一种很有应用前景的可再生、环境友好的能源, 也被认为是最有潜力的储能和转化方法之一. 为了实现高效和经济的水电解, 必须制备高活性、低成本和合适的析氧反应(OER)电催化剂. OER是水分解的半反应, 由于具有四电子-质子耦合的转移过程, OER反应具有更高的超电势. 因此, 它决定了整个水分解系统的整体效率. 虽然某些贵金属及其氧化物(IrO_2或RuO_2)具有较高的OER活性和较低的过电位, 但这些材料的稀缺性和高成本严重限制了它们的大规模应用. 相反, 过渡金属及其衍生物, 例如钴、镍和铁, 由于价格低廉且地壳中含量丰富, 因此是理想的电催化剂材料. 通常, 有两个主要途径可制备高活性OER电催化剂. 一种方法是赋予结构优势, 例如较大的比表面积、合理的孔径和丰富的活性位点; 二是调节反应部位的电子结构, 增强电化学活性. 金属有机框架(MOF)的发展为水分解用非贵金属催化剂的设计提供了新的机会和平台, 因为MOF的天然多孔结构可以促进基质或产物扩散并显著加速电荷转移. 同时, MOF大的比表面积可均匀地暴露其活性位点, 这为制备高性能OER电催化剂提供了良好的模板或前体. 然而, 目前报道的大多数MOF系统仍然存在一些重大问题, 包括导电性差和结构上隐藏的金属中心, 这严重阻碍了它们在电化学过程中的直接利用. 此外, 一些研究表明Dy和Ni自旋是铁磁耦合的, 它可以增加铁的磁性并改变过渡金属基催化剂表面的粗糙度, 但是相对较少的工作集中在其OER应用上.

本文成功地在碳布上通过简单的两步水热法制备了三维结构的铁镝氧化物原位调控的MOF-Ni阵列(FeDy@MOF-Ni/CC). 电化学研究表明, 优化的FeDy@MOF-Ni/CC催化剂仅需251 mV的低过电位即可达到10 mA cm^{-2}, 并具有52.1 mV dec^{-1}的小Tafel斜率. 另外, 在1.0 M KOH中连续测试80 h后, 稳定性仅下降了5.5%. 此外, 在全水分解系统中仅需1.57 V的电池电压即可达到10 mA cm^{-2}, 远远优于大多数先前报道的催化剂. 研究认为, 独特的3D菱形结构以及Fe-Dy-Ni物种的耦合协同作用赋予了其出色的催化性能.

本文采用红外光谱(FTIR)、拉曼光谱、热重分析(TGA)、比表面积测试和X射线光电子能谱(XPS)等表征手段研究了不同催化材料性能变化的原因. 采用FTIR研究了相关材料的表面官能团, 揭示出FeDy@MOF-Ni具有Fe@MOF-Ni和Dy@MOF-Ni典型的特征峰. 此外, FeDy@MOF-Ni的拉曼光谱由Dy@MOF-Ni和Fe@MOF-Ni整合构成. 同时, 不同催化剂的TGA显示出不同的质量变化. 这种明显的差异证明了两步水热法将Dy和Fe物种成功地掺杂到MOF-Ni中. 比表面积测试结果表明, FeDy@MOF-Ni材料具有III型等温线特征, 孔隙尺寸在30–50 nm范围内, 与MOF-Ni前驱体显著不同, 进一步说明MOF-Ni的解离和FeDy@MOF-Ni的成功制备. 采用XPS进一步表征了Fe-Dy氧化物的掺杂对催化剂组成和表面化学态的影响, 发现FeDy@MOF-Ni具有最低的Ni^{2+}/Ni^{3+}和Fe^{2+}/Fe^{3+}比值和Dy结合能负移, 表明不同物种之间存在较强的电子相互作用.

关键词: 金属有机框架; 氧化镝; 协同效应; 析氧反应; 水分解

收稿日期: 2020-02-26. 接受日期: 2020-03-31. 出版日期: 2020-11-05.
*通讯联系人. 电子信箱: xlyang@gxnu.edu.cn
#通讯联系人. 电子信箱: baowang@ipe.ac.cn
$通讯联系人. 电子信箱: isimjant@sabic.com
基金来源: 国家自然科学基金(21965005); 广西自然科学基金(2018GXNSFAA294077); 广西高层次人才工程项目(F-KA18015, 2018ZD004); 广西研究生教育创新计划(XYCSZ2019056, YCBZ2019031).
本文的电子版全文由Elsevier出版社在ScienceDirect上出版(http://www.sciencedirect.com/science/journal/18722067).